

## **Magnet-based smart rock for scour depth evaluation of bridge pier**

\*Fujian Tang<sup>1)</sup>, Yizheng Chen<sup>2)</sup>, Yan Tang<sup>3)</sup>, Zhaochao Li<sup>4)</sup>, Hong-Nan Li<sup>5)</sup>, Genda Chen<sup>6)</sup>

*1),5) State Key Laboratory of Coastal and Offshore Engineering, School of Civil Engineering, Dalian University of Technology, Dalian, Liaoning 116024, China*

*2),3),4),6) Department of Civil, Architectural and Environmental Engineering, Missouri University of Science and Technology, Rolla, MO 65401, USA*

*1) [ftang@dlut.edu.cn](mailto:ftang@dlut.edu.cn)*

### **ABSTRACT**

An algorithm to localize the position of a smart rock was developed and validated in this study. The smart rock is used to monitor the scour depth near a bridge pier or abutment which is a super strong magnet embedded in a concrete ball. It works as two purposes: first, it can automatically rolled down to the scour hole to determine the maximum scour depth; second, the outside concrete layer work as an amour to protect the super magnet from damage from flowing debris, rock during heavy floods. To track the change of the location of the smart rock during a flood event, an algorithm was developed based on the theory of magnetic field interference. Validation tests were conducted at an open area, and results showed that the algorithm could effectively track the location of the smart rock.

### **1. INTRODUCTION**

Scour is the excavation and removal of local river bed around a bridge pier or abutment, due to the erosive action of flowing water during flood events. Progressive removal of river bed at the pier or abutment would impair the integrity of the entire bridge, resulting in bridge instability and potential failure. Scour and other hydraulic induced failures accounted for 58% of all bridge failures in the U.S. (Lagasse et al, 1997), and resulted in loss of human lives and hundreds of millions of dollars. For example, ten people were killed due to the collapse of the I-90 Bridge over the Schoharie Creek in New York in 1987 when a pier footing was damaged by a scour hole (NTSB, 1987). The collapse of I-5 Bridge over the Arroyo Pasajero River in California in 1995 killed 7 people due to the formation of a 3.0 m scour hole (NTSB 1989; Arneson et al, 2012). It was reported that the repair cost for bridges due to scour damage was estimated to be \$300 million in the 1980s (Butch, 1996).

Many techniques or methods have been developed to combat bridge scour effects, including hydraulic countermeasures, structural countermeasures and monitoring techniques. Monitoring is considered as one cost-effective and practical

measure for scour critical bridges by Federal Highway Administration's Hydraulic Engineering Circular N. 23 (HEC-23) (Lagasse et al, 2009). The HEC-23 also classified monitoring instruments into fixed instrumentation, portable instrumentation, and visual inspection. Fixed instrumentation includes sonar, magnetic sliding collar, tilt meter, float-out device, sounding rods, time domain reflectometers (TDR), and so on. Portable instrument typically consists of four components for measurement: an instrument for making the measurement, a system for deploying the instrument, a method to identify and record the horizontal position of the measurement, and a data-acquisition/storage device.

Each method has its advantages and drawbacks. For example, ground penetrating radar and sonar device monitor the profile of the river bed through the transmission and reflection of an electromagnetic radiation or a wave. However, the results are sensitive to noise and difficult to interpret especially when the water contains high concentration sediments, debris or rocks in a flooded river (Park, 2004; Mason 1994; Hayes 1995). Magnetic sliding collar (MSC) monitors the scour depth through the movement of the collar, which slides down the magnetic rod as the deposits around the foundation is eroded away (Schall et al, 1997; Lu et al, 2008). However, the depth monitored from MSC does not usually represent the maximum scour depth. A tilt meter detects the scour-related settlement of a pier or abutment foundation (Avila et al, 1999; Zarafshan et al, 2011). However, it is difficult to differentiate the movement caused by scour and other factors such as traffic, thermal, wind and ambient perturbations. Over the past decades, fiber optic sensors have been used to monitor the scour effects, which were indirectly detected by monitoring strain/deformation change of the FBG sensors due to scour effects (Lin et al, 2004, 2005, 2006; Manzoni et al, 2010, 2011; Zarafshan et al, 2011).

In a previous study, the concept of smart rock technology was proposed to monitor bridge scour effects, particularly for the maximum scour depth (Chen et al, 2015). The smart rock was essentially a small magnet encased in a plastic ball. Calibration tests were conducted and a series of curves were developed which was used to localize the position of the smart rock. However, this localization method is time-consuming and the calibration curves are dependent on the ambient magnetic field which limits its wide application in engineering practice. In this study, an algorithm based on the magnetic field interference was developed to localize the position of smart rock, and its performance was validated at an open area.

## **2. THEORY OF MAGNETIC FIELD AND LOCALIZATION ALGORITHM**

For engineering applications, the smart rock would be deployed with other real rocks in the scour critical zone near the bridge pier. During a flood event, it would roll down to the hole developed due to scour effect. By tracking the change in the location of the smart rock, particularly in the vertical direction, the maximum scour depth could be monitored. To fulfill this purpose, an algorithm needs to be developed to track the location of smart rock based on the theory of magnetic field interference.

Fig. 1 shows a cylinder magnet with  $2a$  in diameter and  $2b$  in height in a cylindrical coordinate system. The origin is located at the centroid of the magnet,  $y$ -axis is the direction from the south pole to the north pole of the magnet, and  $\rho$ -axis represents the radial direction perpendicular to  $y$ -axis.

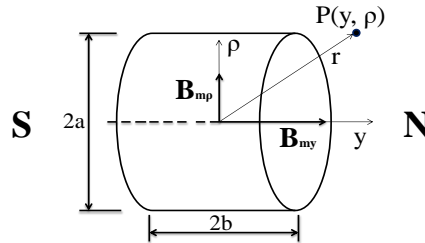


Fig. 1 A cylinder magnet in a cylindrical coordinate system.

The magnetic field is axially symmetrical, and can be represented by a vector  $\mathbf{B}_m$  ( $y, \rho$ ) at point  $P$ . When point  $P$  is significantly far away from the magnet, the magnitudes of longitudinal component  $B_{my}$  and radial component  $B_{m\rho}$  can be expressed by (Derby and Olbert, 2010):

$$\begin{cases} B_{my}(y, \rho) = k \frac{(2y^2 - \rho^2)}{r^5} \\ B_{m\rho}(y, \rho) = k \frac{3\rho y}{r^5} \end{cases} \quad (1)$$

where  $k = \mu_0 \mu / 4\pi$ ,  $\mu_0$  is the permeability of vacuum in T·m/A, and  $\mu$  is the magnetic moment. The magnitude of the total magnetic field intensity is:

$$B_m(y, \rho) = \sqrt{B_{my}^2(y, \rho) + B_{m\rho}^2(y, \rho)} \quad (2)$$

For engineering applications, the magnetic field distribution in the cylindrical coordinate system in Fig. 1 needs to be transferred into a Cartesian coordinate system as shown in Fig. 2. For transition purpose, two Cartesian coordinate system are used: the local coordinate system and the global coordinate system. The origin of the local Cartesian coordinate system ( $p$ -xyz) is located at the center of the magnet, and the  $y$ -axis is pointing from the south pole to the north pole of the magnet.

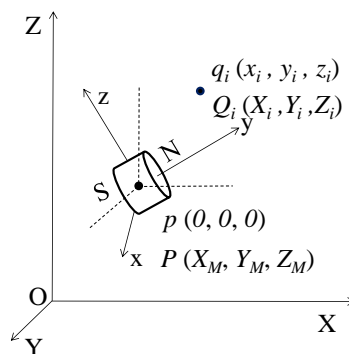


Fig. 2 Global and local coordinate systems.

In the global Cartesian coordinate system (O-XYZ), Y direction is pointing to the south pole of the Earth (the north pole of the geomagnetic field), X-axis is pointing to the west of the Earth, and Z direction is pointing upward following the right-hand rule. Therefore, the magnet center  $p$  (0, 0, 0) in local coordinate system corresponds to point  $P$  ( $X_M, Y_M, Z_M$ ) in global coordinate system, and an arbitrary point  $Q$  has a local coordinate  $q_i$  ( $x_i, y_i, z_i$ ) and a global coordinate  $Q_i$  ( $X_i, Y_i, Z_i$ ).

In local coordinate system, the intensity vector of the magnetic field at point  $q_i$ ( $x_i, y_i, z_i$ ) can be expressed as  $\mathbf{B}_i = (B_{xi}, B_{yi}, B_{zi})$ . Its two components in cylindrical coordinate system are given in Eq. (1), in which the radial component can be further decomposed into x- and z-components. Therefore, the x-, y- and z-components of the magnetic intensity at point  $q_i$  in local coordinate system are

$$\begin{cases} B_{xi} = k \frac{3x_i y_i}{r_i^5} \\ B_{yi} = k \frac{2y_i^2 - x_i^2 - z_i^2}{r_i^5} \\ B_{zi} = k \frac{3z_i y_i}{r_i^5} \end{cases} \quad (3)$$

where

$$r_i = \sqrt{x_i^2 + y_i^2 + z_i^2} \quad (4)$$

To transfer from local coordinate system to global coordinate system, a transition matrix is derived

$$\mathbf{R} = \begin{bmatrix} \cos \beta \cos \gamma & \cos \beta \sin \gamma & -\sin \beta \\ \sin \alpha \sin \beta \cos \gamma - \cos \alpha \sin \gamma & \sin \alpha \sin \beta \sin \gamma + \cos \alpha \cos \gamma & \sin \alpha \cos \beta \\ \cos \alpha \sin \beta \cos \gamma + \sin \alpha \sin \gamma & \cos \alpha \sin \beta \sin \gamma - \sin \alpha \cos \gamma & \cos \alpha \cos \beta \end{bmatrix} \quad (5)$$

where  $\alpha \in [0, 2\pi]$ ,  $\beta \in [0, 2\pi]$ ,  $\gamma \in [0, 2\pi]$  are the rotation angles of the x-, y-, and z-axis in local coordinate system with respect to the X-, Y-, and Z-axis in the global coordinate system. Then, the coordinates transfer between the two systems can be expressed as

$$\begin{pmatrix} x_i \\ y_i \\ z_i \end{pmatrix} = \mathbf{R} \cdot \begin{pmatrix} X_i - X_M \\ Y_i - Y_M \\ Z_i - Z_M \end{pmatrix} \quad (6)$$

Thus, the three-components of the magnetic intensity at any point  $Q_i$  ( $X_i, Y_i, Z_i$ ) in the global Cartesian coordinate system takes the form

$$\begin{pmatrix} B_{xi} \\ B_{yi} \\ B_{zi} \end{pmatrix} = \mathbf{R}^{-1} \begin{pmatrix} B_{xi} \\ B_{yi} \\ B_{zi} \end{pmatrix} = \mathbf{R}^{-1} \begin{pmatrix} k \frac{3x_i y_i}{r_i^5} \\ k \frac{2y_i^2 - x_i^2 - z_i^2}{r_i^5} \\ k \frac{3z_i y_i}{r_i^5} \end{pmatrix} \quad (7)$$

The purpose of the algorithm is to localize the smart rock based on the change of the total magnetic field (TMF) before and after introducing the smart rock. In this study, the magnetic field at a site before introducing a smart rock is called the ambient magnetic field (AMF). In most cases, the AMF is the geomagnetic field and can be expressed as:

$$\mathbf{B}_E = (0, -B_E \cos \theta, -B_E \sin \theta) \quad (8)$$

where  $B_E$  and  $\theta$  are the intensity and dip angle of the geomagnetic field at the test site, respectively. According to the summation principle, the TMF intensity at any point after introducing a smart rock can be expressed as:

$$B_{Ti} = \sqrt{(B_{xi})^2 + [B_{yi} + (-B_E \cos \theta)]^2 + [B_{zi} + (-B_E \sin \theta)]^2} \quad (9)$$

Therefore, the TMF intensity  $B_{Ti}$  is a function of the location ( $X_M, Y_M, Z_M$ ) and its rotation angles ( $\alpha, \beta, \gamma$ ) of the smart rock corresponding to the X-, Y- and Z-axis in the global coordinate system.

Assume there are  $N$  measurements of the TMF intensity  $B_{Ti}^{(M)}$  ( $i = 1, 2, \dots, n$ ) at  $N$  points around the smart rock, and the location of these measured points ( $X_i, Y_i, Z_i, i = 1, 2, \dots, n$ ) are known. At each point, the predicted intensity  $B_{Ti}^{(P)}$  can be calculated by substituting  $X_i, Y_i, Z_i$  in Eq. (7) to (9). Since the measured intensity  $B_{Ti}^{(M)}$  is already known, then there is an error between the predicted and the measured intensities, which is defined as an error function:

$$J(X_M, Y_M, Z_M, \alpha, \beta, \gamma) = \sqrt{\sum_{i=1}^n [B_{Ti}^{(P)} - B_{Ti}^{(M)}]^2} \quad (10)$$

By minimizing the error function in Eq. (10), the location and direction (associated with the rotation angles) of the smart rock can be determined using the sequential quadratic programming (SQP) algorithm (Boggs and Tolle, 1989).

### 3. VALIDATION TEST

Since the purpose of this study is to characterize and validate the smart rock, it is not necessary to cast the outside concrete, and only the prototypes was used. Fig. 3 shows the magnet used in this study, which was a Grade N42 neodymium-iron-boron ( $\text{Nd}_2\text{Fe}_{14}\text{B}$ ) cylindrical magnet with a diameter of 101.6 mm and a height of 50.8 mm,

the maximum residual induction is 1.32 tesla. It was placed in a plastic container with sand and its direction can be adjusted manually during validation test.



Fig. 3 Smart rock prototype used in this study.

The validation tests were conducted at an open area as shown in Fig. 4a. The intensity and dip angle of the geomagnetic field was determined to be  $B_E = 52342$  nT and  $\theta = 67.7^\circ$ . To consider the effect of elevation, wooden poles with different heights ranging from 0.45 m to 1.43 m were fixed at the measurement points (Fig. 4b), and then the sensor head of the magnetometer was placed on the wooden pole to capture the intensity of the total magnetic field.

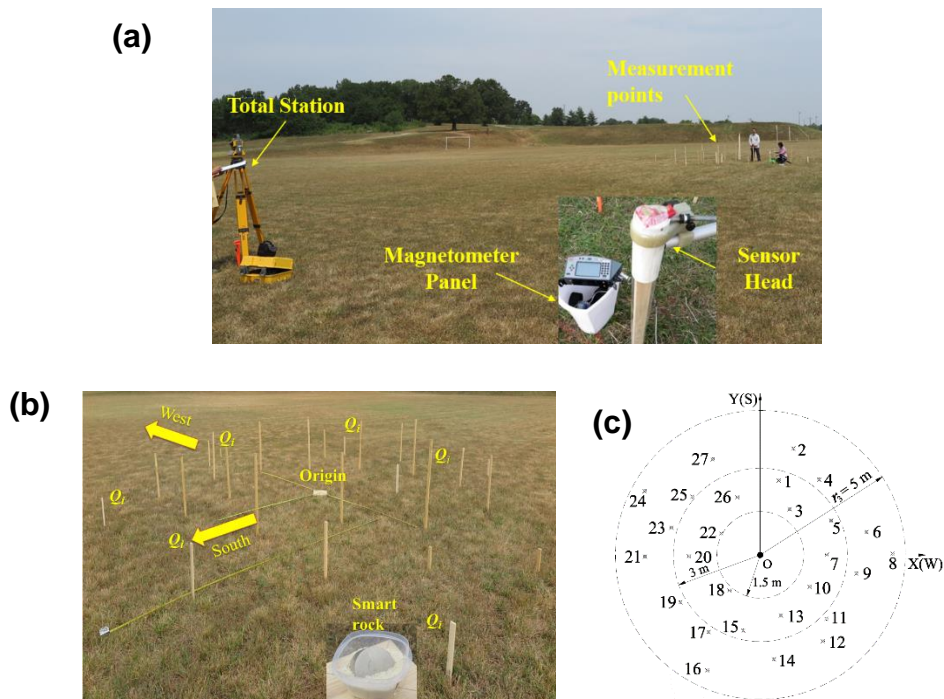


Fig. 4 Test setup and layout: (a) open area test set-up; (b) layout of measurement points; (c) measurement points in the global coordinate system.

The smart rock was placed at the origin of the Cartesian Coordinate XYZ displayed in Figs. 4b and 4c. A total of 27 points  $Q_1, Q_2, Q_3 \dots, Q_{25}, Q_{26}$  and  $Q_{27}$  were selected inside a ring area surrounded by two circles with diameters of 1.5 m and 5.0 m, respectively, as shown in Fig. 4c. The coordinates of the origin and the 27 points were determined by using a total station (Fig. 4a). A magnetometer G858 was used to determine the magnitude of the magnetic field.

To consider the effect of the direction of the smart rock, three orientations of the smart rock were considered and manually adjusted as shown in Fig. 5 including OR1, OR2 and OR3. Therefore, a total of four rounds of measurements were carried out at these 27 points. First, the geomagnetic field were determined at these points with the magnetometer before taking the smart rock to the test site. Next, the smart rock was placed at the origin directing to OR1, and the magnitude of the TMF at the 27 points were recorded. Then the smart rock was pointing to OR2, the magnitude of the TMF were measured again. Finally the smart rock was pointing to OR3, the magnitude of the TMF were recorded.

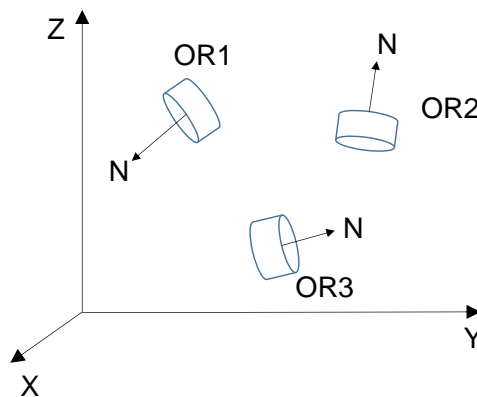


Fig. 5 Three orientations of AOS during the single point positioning test: OR1, OR2 and OR3.

Table 1 and Table 2 show the comparison of the test results of the smart rock between its actual location (origin point in the coordinate system)/direction and the predicted location/direction using the algorithm in Eq. (10), when the smart rock pointed to three directions OR1, OR2, and OR3. The direction of the smart rock can be calculated based on the rotation angles:

$$\frac{\vec{B}}{\|\vec{B}\|} = \begin{pmatrix} i \\ j \\ k \end{pmatrix} = \begin{pmatrix} \sin \alpha \sin \beta \cos \gamma - \cos \alpha \sin \gamma \\ \sin \alpha \sin \beta \sin \gamma + \cos \alpha \cos \gamma \\ \sin \alpha \cos \beta \end{pmatrix} \quad (11)$$

It can be seen that the predicted location/direction are very close to the actual location/direction of the smart rock in three directions. The error of the localization algorithm can be evaluated by the root of sum of squares (RSS) principle:

$$RSS_{(X,Y,Z)} = \sqrt{\left[ (X^P - X^M)^2 + (Y^P - Y^M)^2 + (Z^P - Z^M)^2 \right]} \quad (12)$$

$$RSS_{(i,j,k)} = \sqrt{\left[ (i^P - i^M)^2 + (j^P - j^M)^2 + (k^P - k^M)^2 \right]} \quad (13)$$

where  $(X^P, Y^P, Z^P)$  and  $(X^M, Y^M, Z^M)$  are the predicted and the measurement coordinates of the AOS smart rock,  $(i^P, j^P, k^P)$  and  $(i^M, j^M, k^M)$  are the predicted and the measured three-components of the directions of the smart rock, respectively. As shown in Table 1 and Table 2, the SRSS error for the location of the smart rock for all three cases are 0.01 m, which is enough for engineering applications. The error for the predicted orientation of the smart rock is smaller than 0.02 rad.

Table 1. Predicted and measured coordinates of smart rock (unit: m)

Case	OR1 (X, Y, Z)	OR2 (X, Y, Z)	OR3 (X, Y, Z)
Measured	(0.00,0.00,0.00)	(0.00,0.00,0.00)	(0.00,0.00,0.00)
Predicted	(-0.01, 0.00, 0.01)	(0.00,0.00,-0.01)	(0.00,0.01,-0.01)
RSS	0.01	0.01	0.01

Table 2. Predicted and measured orientation of smart rock (unit: rad.)

Case	OR1 (i, j, k)	OR2 (i, j, k)	OR3 (i, j, k)
Measured	(0.55,-0.51,-0.66)	(-0.47,0.24,0.85)	(0.46,0.86,0.22)
Predicted	(0.56,-0.52,-0.64)	(-0.47,0.23,0.85)	(0.47,0.86,0.21)
RSS	0.02	0.01	0.01

#### 4. CONCLUSIONS

In this study, an algorithm was developed to localize the position of the smart rock, which would be used to monitor the scour depth of bridge piers or abutment during flood events. The distribution of the magnetic field of a cylinder magnet was derived and was incorporated into the total magnetic field after considering the AMF (geomagnetic field in most cases). The localization of the position of the smart rock was realized by minimizing the difference between the measured and the predicted total magnetic field intensity. Validation tests were conducted at an open area, and results showed that the algorithm can successfully localize the position and its orientation of the smart rock. The RSS error is 0.01 m which is enough for engineering applications.



## ACKNOWLEDGEMENTS

Financial support for this study was provided by the Fundamental Research Funds for the Central Universities of China under No. DUT17RC(3)076, by the innovative research group of the National Natural Science Foundation of China under No. 51421064, and by the U.S. Department of Transportation Office of the Assistant Secretary for Research and Technology under Cooperative Agreement No. OASRTRS-14-H-MST.

## REFERENCES

- Arneson, L.A., Zevenbergen, L.W., Lagasse, P.F., and Clopper, P.E. (2012). "Hydraulic Engineering Circular No.18: Evaluating Scour at Bridges." *5th Edition, U.S. Department of Transportation, Federal Highway Administration, Publication No. FHWA-HIF-12-003.*
- Avila, C. M. C., Racin, J. A., and Davies, P. (1999). "Talk to your bridges and they will talk back—Caltrans bridge scour monitoring program." *Proc., ASCE Hydraulic Conf., ASCE, New York.*
- Boggs PT and Tolle JW, (1989). "A strategy for global convergence in a sequential quadratic programming algorithm", *SIAM J. Numerical Analysis* **26**(3) 600–623.
- Butch, G.K. (1996). "Evaluation of selected instruments for monitoring scour at bridges in New York." *North American Water and Environment Congress, ASCE.*
- Chen, G., Schafer, B.P., Lin, Z., Huang Y., Suaznabar O., Shen J., and Kerenyi K. (2015) "Maximum scour depth based on magnetic field change in smart rocks for foundation stability evaluation of bridges." *Structural Health Monitoring* **14**(1), 86-99.
- Derby N and Olbert S (2010). "Cylindrical magnets and ideal solenoids", *American Journal of Physics* **78**(3) 229–235.
- Hayes, D. C., and Drummond, F. E. (1995). "Use of fathometers and electrical-conductivity probes to monitor riverbed scour at bridges and piers." *Water Resource Investigations Rep. No. 94-4164, U.S. Geological Survey, Hartford, Connecticut.*
- Lagasse, P.F., Richardson, E.V., Schall, J.D., and Price, G.R. (1997). "Instrumentation for measuring scour at bridge piers and abutments." *NCHRP Report 396: TRB, National Research Council, Washington, D.C..*
- Lagasse, P. F., Clopper, P. E., Pagán-Ortiz, J. E., Zevenbergen, L. W., Arneson, L. A., Schall, J. D., and Girard, L. G. (2009). "Bridge scours and stream instability countermeasures: experience, selection and design guidance." *Hydraulic Engineering Circular No. 23, Volume I, FHWA NHI HEC-23, Department of Transportation, Federal Highway Administration, Washington, D.C..*
- Lin, Y. B., Chang, K. C., Lai, J.-S., and Wu, I.-W. (2004). "Application of optical fiber sensors on local scour monitoring." *Proc., IEEE Sensors, Vol. 2, Vienna, Austria, 832–835.*
- Lin, Y. B., Chen, J.-C., Chang, K.-C., Chern, J.-C., and Lai, J.-S. (2005). "Real-time monitoring of local scour by using fiber Bragg grating sensors." *Smart Material and Structures*, **14**(4), 664–670.

- Lin Y.B, Lai J.S, Chang K.C and Li L.S. (2006), "Flood Scour Monitoring System Using Fiber Bragg Grating Sensors". *Smart mater. Struct.*, **15**(6), 1950-1959.
- Lu, J.Y., Hong, J.H., Su, C.C., Wang, C.Y., and Lai, J.S. (2008). "Field measurements and simulation of bridge scour depth variation during floods." *J. Hydra. Eng.*, **134**(6), 810–821.
- Manzoni, S., Crotti, G., Cigada, A., Inzoli, F., and Ballio, F. (2010) "Monitoring bridge scour by Bragg grating array." *Scour and Erosion: Proceedings of 5th International Conference on Scour and Erosion*, ASCE, November 7-10, 2010, San Francisco, CA.
- Manzoni, S., Crotti, G., Ballio, F., Cigada, A., and Colombo, E. (2011) "BLESS: A fiber optic sedimenter." *Flow Measurement and Instrumentation*, **22**(5), 447–455.
- Mason, R. R., and Shepard, D. M. (1994). "Field performance of an acoustic scour-depth monitoring system." *Proc., Fundamentals and Advancements in Hydraulic Measurements and Experimentation*, New York, 366–375.
- N.T.S.B. (1987). "Collapse of New York Thruway (I-90) Bridge, Schoharie Creek, near Amsterdam, New York, April 5, 1987." NTSB Number: HAR-88/02, NTIS Number: PB88-916202.
- N.T.S.B. (1989). "Collapse of the northbound U.S. Route 51 Bridge spans over the Hatchie River, near Covington, Tennessee, April 1, 1989." NTSB Number: HAR-90/01, NTIS Number: PB90-916201.
- Park, I., Lee, J., and Cho, W. (2004). "Assessment of bridge scour and riverbed variation by ground penetrating radar." *Proc., 10<sup>th</sup> Int. Conf. on Ground Penetrating Radar, GPR 2004*, Delft, The Netherlands, 411–414.
- Schall, J.D., G.R. Price, G.A. Fisher, P.F. Lagasse, and E.V. Richardson (1997b). "Magnetic Sliding Collar Scour Monitor – Installation, Operation and Fabrication Manual." *NCHRP Report 397B, Transportation Research Board, National Research Council, National Academy Press*, Washington, D.C.
- Zarafshan, A., Iranmanesh, A., and Ansari, F. (2011). "Vibration-based method and sensor for monitoring of bridge scour." *J. Bridge Eng.*, **17**(6), 829-838.